DEVELOPMENT OF DIAGNOSTICS AND DATA ANALYSIS ON ASDEX IN 1988

IPP III / 148 June 1989

MAX-PLANCK-INSTITUT FÜR PLASMAPHYSIK

8046 GARCHING BEI MÜNCHEN

MAX-PLANCK-INSTITUT FÜR PLASMAPHYSIK

GARCHING BEI MÜNCHEN

DEVELOPMENT OF DIAGNOSTICS AND DATA ANALYSIS ON ASDEX IN 1988

IPP III / 148 June 1989

Die nachstehende Arbeit wurde im Rahmen des Vertrages zwischen dem Max-Planck-Institut für Plasmaphysik und der Europäischen Atomgemeinschaft über die Zusammenarbeit auf dem Gebiete der Plasmaphysik durchgeführt.

DEVELOPMENT OF DIAGNOSTICS AND DATA ANALYSIS ON ASDEX IN 1988

CONTENTS

CONTENTS

2.1 Diagnostic Development

2.1.1 Non-Doppler broadening mechanisms of CXRS emission profiles and their contributions to ion temperature measurements (J.V. Hofmann)

Charge exchange recombination spectroscopy (CXRS) has been developed into a very successful diagnostic tool in tokamak devices where high-energy neutral injectors are applied for additional heating. The well-known charge exchange reaction leads to photon emission in the UV and visible ranges which are most suitable for ion temperature measurement based on Doppler broadening of the profiles. The emission results from $\Delta n = 1$, $\Delta l = 1$ transitions of highly excited Rydberg states. In this context we considered contributions from fine-structure splitting of the generally unresolved l-levels of a transition, the Zeeman splitting in the magnetic field of the tokamak and the translational Stark effect due to the v×B field of the ions, which may have a non-negligible influence on the total broadening of the observed transition. We elucidate these effects by referring to H-like $^{8}O^{7+}$ and Na-like $^{36}Kr^{25+}$ ions, which are sufficiently different in mass and charge. The visible transitions of these two ions and their population structures have been carefully analyzed in ASDEX.

Fine-structure contributions: We first calculate the intensities of all $\Delta l = \pm 1$ transitions within an observed $\Delta n = 1$ emission line. Next we assign to each transition a Doppler profile and obtain by superposition the total emission profile. To this profile we fit a single Gaussian to deduce a fit temperature.

Applying this procedure for several temperatures as input (T = 0.5 - 6.0 keV), our calculations yield a linear dependence between the true and fit temperatures with a slope very close to 1 but with a positive off-set for the fit temperature. For the n = 17-16 transition of Kr^{25+} (λ = 302.11 nm) this off-set is as large as $T_{fit} - T_{true}$ = 1.7 keV. This clearly demonstrates the importance of the additional fine-structure broadening in this case. In the case of the O^{7+} n = 10-9 (λ = 606.83 nm) transition this contribution is markedly reduced to 0.16 keV.

Zeeman and Stark effects: These contributions are estimated for ASDEX conditions (B = 2 T) for the observed $\Delta n = 1$ transitions. Strictly speaking, we have to consider the anomalous Zeeman effect for each unresolved fine-structure transition. However, for high orbital momenta l and $j = l \pm 1/2$ the Landé g-factor is always close to 1. In this case the anomalous

Zeeman effect can be approximated by the normal Zeeman effect to yield triplets with a total energy splitting of $\Delta E = 2\mu_B B$, where μ_B is Bohr's magneton. As a first estimate, we take this splitting into account by assuming an additional equivalent Gaussian broadening. After performing the corresponding convolution with the Doppler profile we find a rather small effect on the fit temperature of the order 1-3 % for both Kr^{25+} and O^{7+}.

The calculated Stark effect is estimated for B = 2 T and T_i = 2 keV, leading to a characteristic electric field strength of $E = 3.0 \cdot 10^5$ V/m for oxygen. In this case we have to consider the splitting of the degenerate j-levels (j = l ± 1/2), which yields 0.8 and 7 % of the fine-structure splitting for the highest and lowest j-levels of the O^{7+} n = 10 state respectively. Since the main contribution to our investigated lines originates from the highest l- and j-states, we conclude that the Stark effect can indeed be neglected.

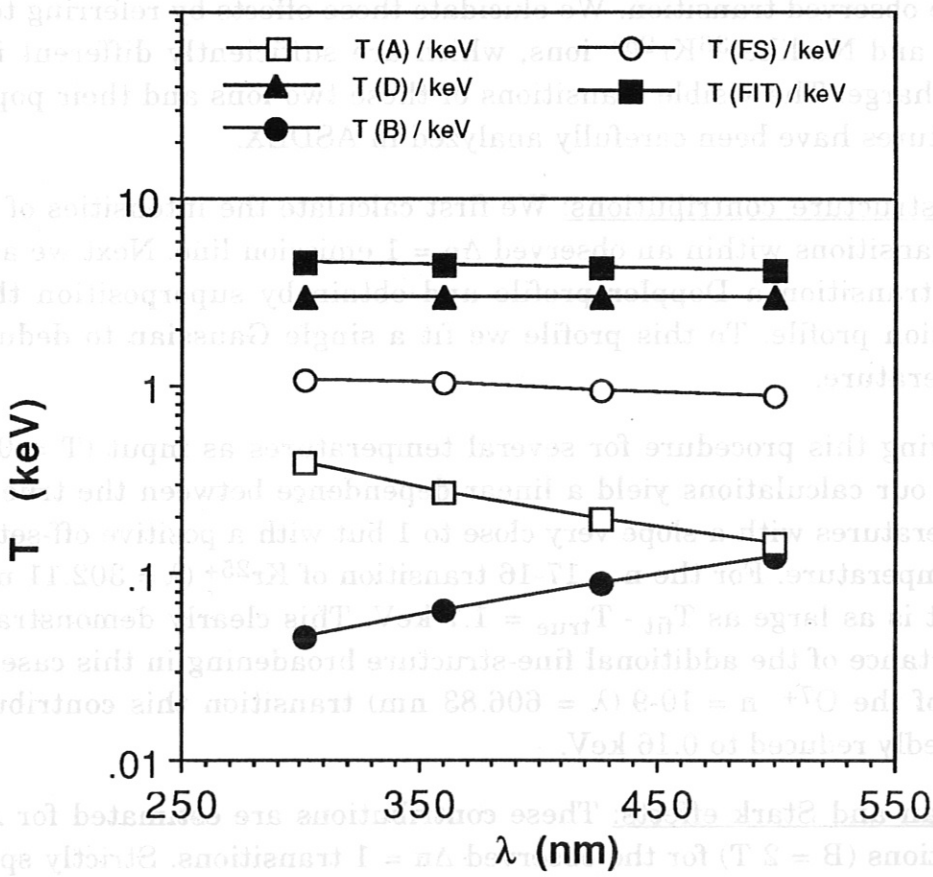

Fig. 1: Contributions to the ion temperature for Kr^{25+}.

Results: In Fig. 1 the contributions to the ion temperature for the visible krypton transitions are plotted. The numerically determined fit temperature (FIT) is assumed to be the sum of the various contributions, namely Doppler (D), fine structure (FS), Zeeman (B) and instrumental broadening (A). Apart from the FS contribution, all terms are known independently. The FS term is thus obtained from $T_{FIT} = T_D + T_{FS} + T_B + T_A$. Clearly, Doppler broadening dominates in all cases but the contribution of the fine structure is already 24 % of the fit temperature.

The different scalings of the additional broadening terms with wavelength together with our observations on ASDEX suggest the O^{7+}, n = 10-9 (λ = 606.83 nm) transition as best suited to ion temperature measurements using CXRS. On the other hand, the Kr^{25+} lines may be more suited to rotation measurements because of a more favourable relation between line shift and broadening.

2.1.2 Charge exchange cross-sections of highly ionized Rydberg atoms (J.V. Hofmann)

Charge exchange recombination spectroscopy (CXRS) is a powerful diagnostic to deduce impurity concentrations from the plasma core region. However, for this kind of diagnostic the cross-sections and rate coefficients for the charge exchange process have to be known. Especially the range of high principal quantum numbers n is of great importance because the resulting transitions are in the UV and visible regions. For low ionic charge numbers Z good agreement between theoretical and experimental data in the range below the resonant principal quantum number n_{res} was found and an extrapolation of the cross-sections σ_n for $n > n_{res}$ as $1/n^3$ seems to hold. For high Z and high quantum states above the resonant level, however, no reliable data are available and several theoretical models show great deviations in the predicted cross-sections. Recent calculations indicate a much stronger decrease than $1/n^3$.

In ASDEX we investigated the absolute values and the dependence of the rate coefficients for CXR on the principal quantum number well above the resonant n_{res} for high-Z and compared them with theoretical calcula-

tions. We investigated UV and visible transitions of Na-like $^{36}Kr^{25+}$ (n = 23-22, ...16-15), Li-like $^{16}S^{13+}$ (n = 15-14,...11-10) and H-like $^{8}O^{7+}$ (n = 10-9,...8-7) ions. With the absolute intensities from these transitions as input, we calculated the rate coefficients for charge exchange and impurity con-centrations using a code by H.P. Summers. For these calculations we used theoretical cross-sections for H-like ions from the UDWA (unitarized distorted wave approximation) model (for S and O), MLZ (multichanel Landau-Zener) model (for Kr) and CCAO (close coupling of atomic orbitals) model (for O) since there are no theoretical data for Na- and Li-like ions available and the UDWA model provides only data up to Z = 14. We therefore chose theoretical MLZ data of H-like $^{26}Fe^{25+}$ to represent $^{36}Kr^{25+}$ and UDWA data of H-like $^{14}S^{13+}$ to represent $^{16}S^{13+}$. These data had to be extrapolated for the high n transitions in the UV and visible ranges. This yields a highly different decay of the cross-sections σ_n in the case of UDWA and MLZ, resulting in a difference of 1-4 orders of magnitude for σ_n as shown in Fig. 2. The extrapolation was done with the

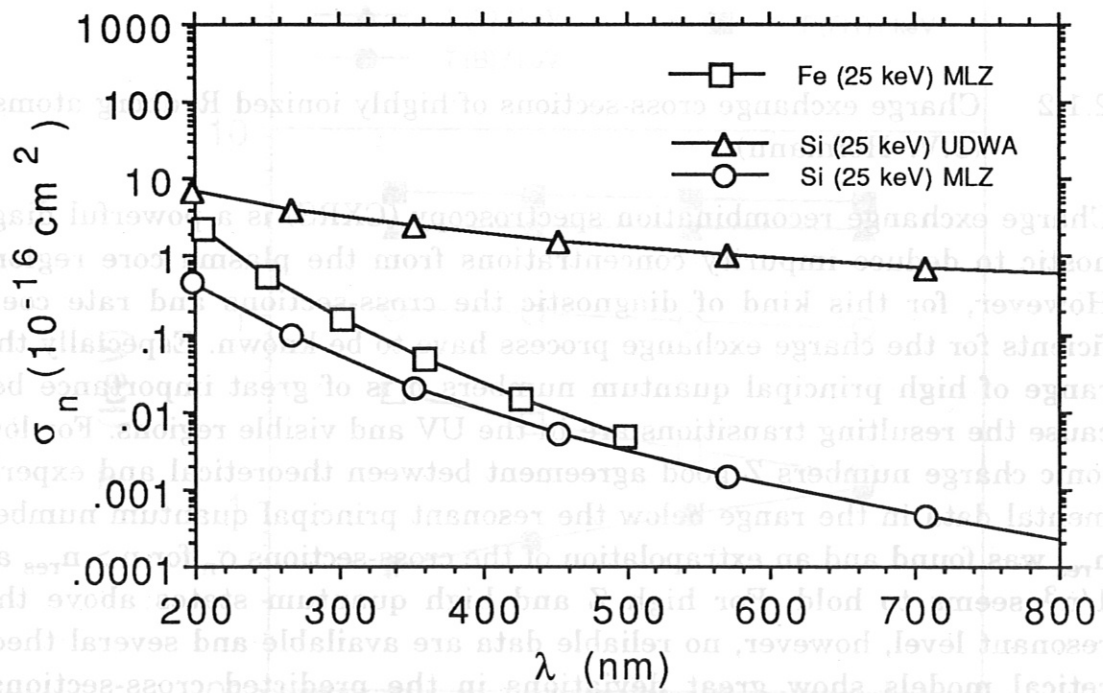

Fig. 2: CXR cross-sections from UDWA and MLZ models as a function of the wavelength of the Δn = 1 transition of the resulting H-like ion for the UV and visible ranges.

assumption of a $1/n^{\alpha}$ decay and α was determined from the last two data points of the data base, respectively.

Results: The rate coefficients deduced from the measured intensities show a nearly exponential decay for the high quantum numbers n in good agreement with the UDWA and CCAO data for S^{13+} and O^{8+}. Furthermore, the absolute values of the rate coefficients are consistent with our measurements. On the other hand, the MLZ data do not agree with our measurements and systematically provide rate coefficients that are of 2-3 orders of magnitude too low. This results from the much too strong decay of the MLZ data for high n. The use of cross-sections for H-like ions cannot account for this strong deviation since the high Rydberg states resulting from CXRS are to a good approximation H-like systems, as shown by the measured wavelength and our calculations.

We therefore conclude that the CXR cross-sections from the UDWA model are an adequate description of these high n states and allow deduction of impurity concentrations from absolutely measured CXR line intensities in the UV and visible ranges. The MLZ model, however, strongly underestimates the $\Delta n = 1$ line intensities in this region.

2.1.3 Impurity gas oscillation experiments for transport studies (K. Krieger, G. Fussmann, G. Janeschitz)

Gaseous impurities are blown into ASDEX discharges with sinusoidal modulation of the gas flow. By harmonic analysis of the line radiation emitted in different ionization stages it is possible to determine the amplitude and phase at the modulation frequency and its higher harmonics. Radial profiles of these quantities are obtained from radial scans in a series of similar discharges. These profiles of amplitude and phase allow determination of the transport coefficients of the respective impurity within the scope of a given theoretical model.

In first experiments silane (SiH_4) and hydrogen sulphide (H_2S) were used. Compared with noble gases, one advantage of these gases is the lack of recycling.

Fig. 3 shows various signals from a gas puffing experiment using H_2S with a modulation frequency of 5 s^{-1} (ASDEX #25739). During the time interval 1.7 s - 2.7 s additional heating with 600 kW neutral injection was applied. The increase of the phase shift with decreasing radius of the respective emission zone is obvious.

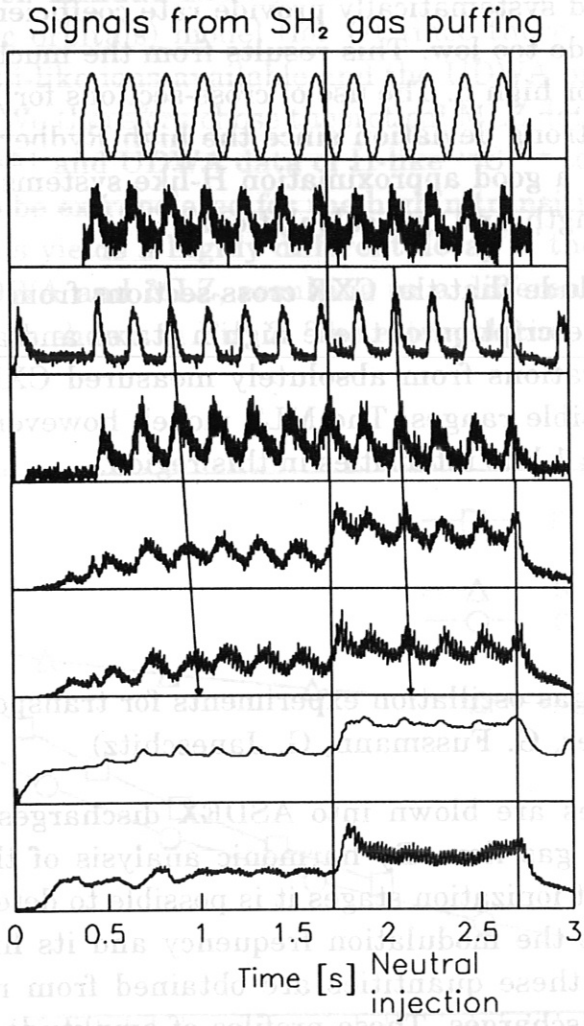

Fig. 3: Signals from gas puffing with sulphurhydrogen (H_2S) during discharge #25739.

Top: valve voltage and actual gas flow.
Middle: S VI, S XIV, S XV and S XVI intensities along central chords.
Bottom: total radiation and soft-X radiation.

Fig. 4 shows the amplitude spectra of the Fourier-transformed signals and the phase shift with respect to the driving voltage of the gas valve at the modulation frequency. Because of the nonlinear response of the piezo valve, higher harmonics occur in the spectra. As the frequency increases the decay of the higher harmonics as a function of radius becomes more pronounced in accordance with theoretical predictions. The reduction of the higher harmonics can also be seen directly from Fig. 3: towards the plasma centre the sine oscillations become broader because of the

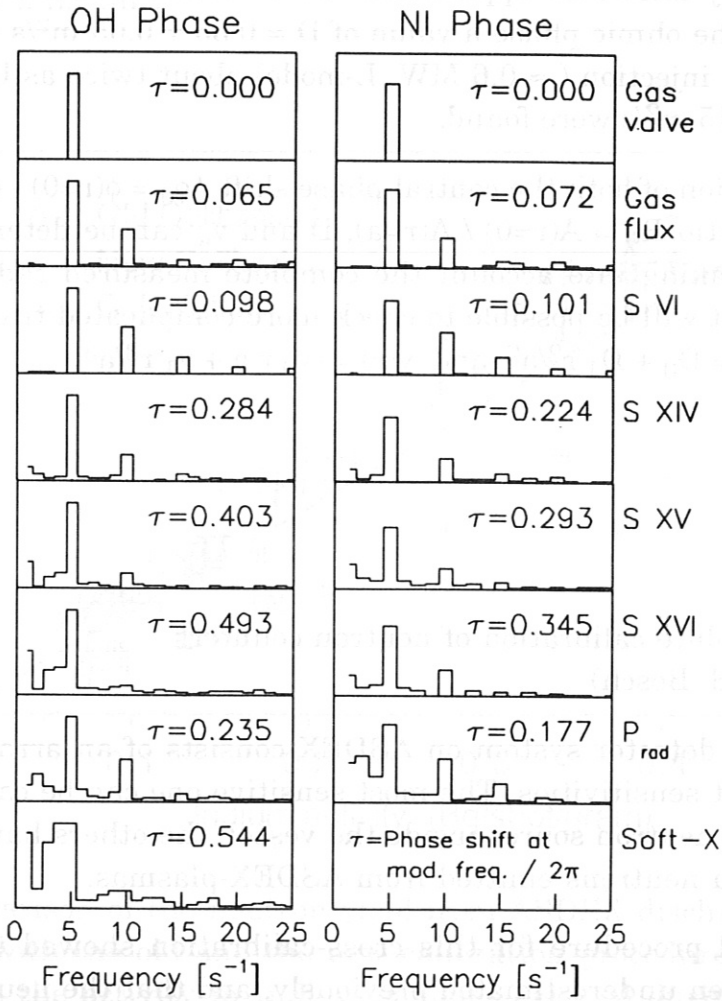

Fig. 4: Amplitude spectra and phase shifts with respect to the voltage of gas valve.

vanishing higher-frequency contributions. One should also note the smaller phase shifts during the NI-heating phase as a result of enhanced diffusion.

To evaluate the experimental data, we tentatively used a simple model for the impurity flux $\Gamma_z = -D\,\partial n_z/\partial r + v\,n_z$, assuming D(r) = const. and v(r) = $-v_a r/a$. Because of uncertainties in the absolute calibrations of the various the impurity flux $\Gamma_z = -D\,\partial n_z/\partial r + v\,n_z$, assuming D(r) = const. and v(r) = $-v_a r/a$. Because of uncertainties in the absolute calibrations of the various instruments we have concentrated so far on the phase shift relation, which already allows an approximate determination of the diffusion coefficient. For the ohmic phase a value of $D \approx 0.35 \pm 0.05$ m^2/s was obtained. With neutral injection (≈ 0.6 MW, L-mode) about twice as large values of $D \approx 0.70 \pm 0.15$ m^2/s were found.

With evaluation of both the central phase shift $\Delta\phi_0 = \phi(r=0) - \phi(r=a)$ and the amplitude ratio $R_0 = A(r=0) / A(r=a)$, D and v_a can be determined simultaneously. Taking into account the complete measured radial profiles of $\Delta\phi_0$ and R_0, it will be possible to check more complicated transport models such as $D(r) = D_0 + D_1\,r^2/a^2$ and $v(r) = -v_0\,r/a + v_1\,r^3/a^3$.

2.1.4 Absolute calibration of neutron counters (H.-S. Bosch)

The neutron detector system on ASDEX consists of an array of detectors with different sensitivities. The most sensitive one can be calibrated absolutely with a neutron source inside the vessel, the others have to be cross-calibrated via neutrons emitted from ASDEX-plasmas.

An improved procedure for this cross-calibration showed that the dead times had been underestimated previously, and that the neutron emission from ASDEX is higher than assumed before by up to 80 %. Fig. 5 shows this change with a comparison of the neutron yield, evaluated with the old calibration procedure as well as with the new one, versus the activity in Indium samples exposed during the same discharges.

During the last opening in summer 88 an absolute calibration of the most sensitive detector was performed, which showed no changes compared to the absolute calibration of 1987. All calibrations have been performed with the neutron source at a major radius of 155 cm. The plasma centre, however, is usually at R = 165 cm, and due to the Shafranov shift even further out. The last calibration indicated that this yields an overestimation in the neutron rate of at least 5-7 % (for R = 165 cm), but for larger radii this has not yet been measured. For Fig. 5 the yields have been reduced by 10 % as a first approximation for highly heated plasmas, but the radius depency of the neutron detector efficiency will have to be measured carefully during the next ASDEX opening.

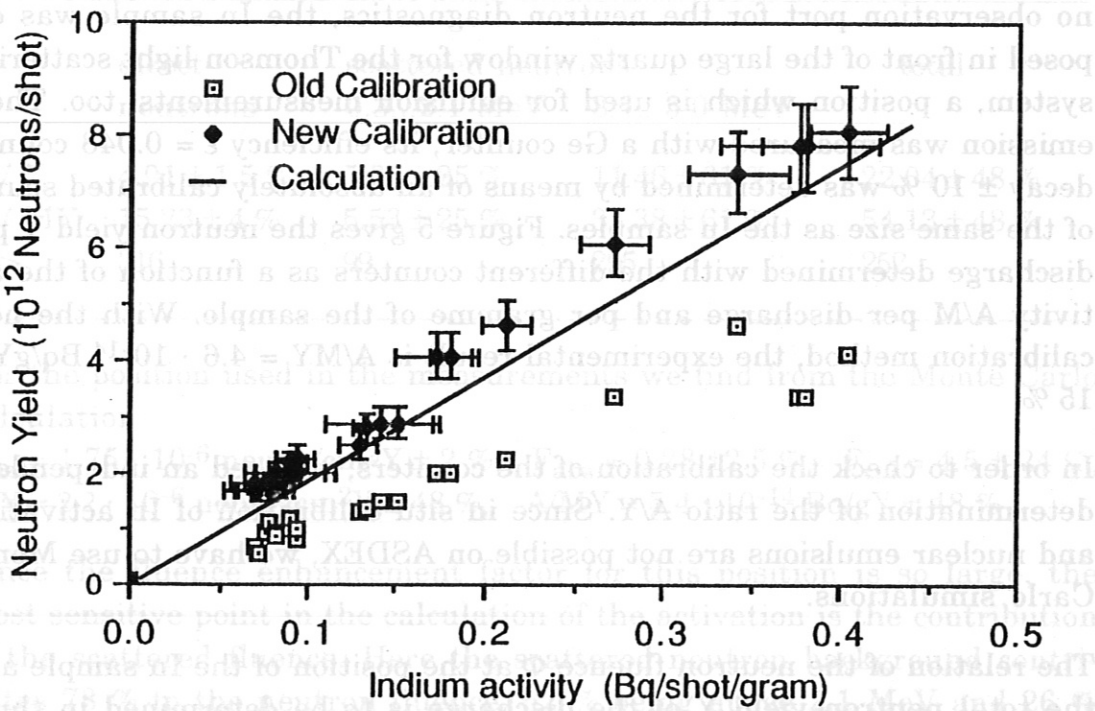

Fig. 5: Comparison of the neutron yield from ASDEX discharges, evaluated with the old and the new calibration procedure. The x-axis shows the activity in Indium-samples exposed during these discharges. The straight line shows the neutron yield calculated from the Indium activity with neutron transport codes (see chapter 2.1.5).

2.1.5 Indium activation studies and Monte Carlo simulation

(R. Bätzner, K. Hübner, L. Ingrosso (Universität Heidelberg), C. van Calker (Universität Düsseldorf), B.V. Robouch (ENEA, Frascati), J. Kucinski (Institute for Nuclear Studies, Otwork-Swierk, Poland), H.-S. Bosch)

Since the in situ calibration of the counter array (see Sect. 2.1.4) could only be done at low neutron rates, it is of great importance that the calibration be independently checked at high yields. This can be done by a yield determination using activation methods or nuclear emulsions. Our intention is to combine the two methods on ASDEX.

For the activation measurements the reaction $^{115}In(n,n')^{115}In^m$ and the subsequent γ emission of $^{115}In^m$ at 335 keV are used. As ASDEX provides no observation port for the neutron diagnostics, the In sample was exposed in front of the large quartz window for the Thomson light scattering system, a position which is used for emulsion measurements, too. The γ emission was measured with a Ge counter, its efficiency $\varepsilon = 0.048$ counts/decay $\pm$ 10 % was determined by means of an absolutely calibrated source of the same size as the In samples. Figure 5 gives the neutron yield Y per discharge determined with the different counters as a function of the activity A/M per discharge and per gramme of the sample. With the new calibration method, the experimental result is $A/MY = 4.6 \cdot 10^{-14}$ Bq/gY $\pm$ 15 %.

In order to check the calibration of the counters, we need an independent determination of the ratio A/Y. Since in situ calibration of In activation and nuclear emulsions are not possible on ASDEX, we have to use Monte Carlo simulations.

The relation of the neutron fluence Φ at the position of the In sample and the total neutron yield Y of the discharge is to be determined in three steps. Firstly, one has to calculate the observed part of the plasma volume and its corresponding neutron fluence $\Phi_0 = \int \{Y(r) / 4\pi s(r)^2\}\, dV = f_{obs} Y$ at the detector position. Here Y(r) is the local source strength and s(r) is the distance between the point of emission and the detector. Secondly, one has to take into account the fluence attenuation factor F_{abs} for the neutron absorption between the plasma and detector. Thirdly, one has to determine the fluence enhancement factor F_{col} caused by the scattered neutron background. So we have $\Phi = \Phi_0 F_{abs} F_{col}$, and the absolute neutron yield is given by $Y = \Phi / f_{obs} F_{abs} F_{col}$.

For ASDEX all three factors are simultaneously determined by neutron migration calculations using the VINIA software. The results of these calculations are used as input for software which simulates the response of the In sample to the incoming neutron fluence and gives the number of activated nuclei N_a in the sample as output. From this number the activity A of the sample is calculated by $A = r_\gamma \lambda N_a$. $r_\gamma = 0.459$ is the number of γ emissions per disintegration. Furthermore, an effective activation cross-section $\langle\sigma\rangle$ is deduced by means of the relation $N_a = N_{In} \Phi \langle\sigma\rangle$, where N_{In} is the total number of ^{115}In nuclei in the sample. - The numerical results for fluence, activation and $\langle\sigma\rangle$ are given in

Table 1: Numerical results
(Φ/Y in 10^{-7} neutr./cm^{2}Y, A/MY in 10^{-15} Bq/gY, $\langle\sigma\rangle$ in mbarn).

	direct neutrons	scattered neutrons 0.3...2.1 MeV	scattered neutrons 2.1...3.0 MeV	total
Φ / Y	4.91 ± 1.5 %	5.68 ± 25 %	11.46 ± 61 %	22.04 ± 48 %
A / MY	15.23 ± 4 %	5.53 ± 25 %	33.38 ± 61 %	54.13 ± 48 %
$\langle\sigma\rangle$	316	99	295	252

For the position used in the measurements we find from the Monte Carlo calculation
$f_{obs} = 1.75 \cdot 10^{-6}$ neutr./cm^{2}Y ± 2 %, $F_{abs} = 0.28$ ±2.5 %, $F_{col} = 4.5$ ± 24 %,
$\Phi/Y = 2.2 \cdot 10^{-6}$ neutr./cm^{2}Y ± 48 %, $A/MY = 5.4 \cdot 10^{-14}$ Bq/gY ± 48 % .

Since the fluence enhancement factor for this position is so large, the most sensitive point in the calculation of the activation is the contribution of the scattered fluence. Here the scattered neutron background contributes 78 % to the neutron fluence, 52 % being above 2.1 MeV and 26 % below. However, the strong decrease of the In activation cross-section below 2 MeV somewhat reduces the relative contribution of the scattered fluence to the activation, so that of the 72 % of the activation caused by the scattered fluence only 10 % comes from the background below 2.1 MeV.

The main problem in Monte Carlo simulations are the large contributions to the scattered background coming from parts of the device which are very close to the detector; in our case the most critical contributors are the quartz window and its flange. They introduce large error bars in the re-

sult. To reduce the statistical fluctuations, a new Monte Carlo procedure was therefore developed and will be used in future.

Within their error bars, the numerical and experimental results for the activity per emitted neutron agree well. In the past we measured the neutron energy spectrum at the position of the In samples by means of nuclear emulsion. This will allow us to check the Monte Carlo calculations in detail. Furthermore, the determination of Φ from the emulsion measurements suffers much less from the scattered background. Here we will use only the energy region above 2.3 MeV, where we have F_{col} = 1.57 ± 4 % and $\Phi/Y = 7.7 \cdot 10^{-7}$ neutr./cm^{2}Y ± 3.5 %. The combination of In activation, nuclear emulsion and Monte Carlo simulation is expected to offer a possibility of checking the counter calibration in situ at high neutron rates.

2.1.6 Heterodyne far-infrared collective scattering (G. Dodel and E. Holzhauer, IPF Stuttgart)

The 119 μm homodyne collective scattering system operating on ASDEX for investigation of density turbulence (cf. Sect. 1.4.6.1) does not yet allow one to determine the propagation direction of the fluctuations. Since the latter is of fundamental interest in connection with the possible existence of η_i-modes, the scattering system was modified to allow heterodyne detection.

For that purpose a CO_2-laser-pumped 119 μm CH_3OH twin laser was constructed. It will allow one to set frequency differences of up to a few megahertz between the scattering laser beam and the local oscillator. The heterodyne system will be used during the experiments in 1989.

2.1.7 High-temperature Langmuir probes (A. Carlson)

To extend the operating range of the scanning Langmuir probes to radii within the separatrix, we built a probe head with tips and body made of graphite. The old probe was constructed from molybdenum, which has similar thermal properties, but a higher Z. Suprathermal electrons, which seem to produce most of the heating of the probe, are thus absorbed much more efficiently in molybdenum. When approaching the plasma too closely, we have often observed thermal electron emission or even melting of the tips. Impurities released upon heating have also often caused disruptions. Initial measurements with the graphite probe have proved that it is very robust, but thermal emission still is a problem.

2.1.8 L_α emission from ionization gauges (M. Lörcher, G. Haas, K.-H. Steuer)

Codes like DEGAS which simulate the interaction of neutral gas with plasma (e.g. in a divertor), not only deliver the global density and flux of neutral particles, but also allow one, in addition, to distinguish between atoms and molecules. Whereas the global parameters of the neutral gas in a divertor can be measured by, for example, special ion gauges like those, which are installed in the divertor chamber, there has until now been no possibility of measuring the atomic and molecular density independently. In the frame of a diploma thesis (M. Lörcher) an ASDEX neutral pressure gauge was modified in such a way that it delivers not only the global density of neutral particles (molecules and atoms) by ionization, but also the density of the atoms by measurement of the L_α-radiation produced by electron impact exitation. Owing to the very weak intensity the main effort was dedicated to developing a detector-filter combination which allows the L_α-radiation to be separated from the H_2 bands in the VUV and be measured with a time resolution of at least a few ms. Several versions were tested theoretically and practically. The best solution was found to be a combination of an O_2 filter using MgF_2 windows and a multichannel plate.

The arrangement was tested and calibrated with an atomic beam of known intensity from an oven. Fig. 6 shows the L_α-radiation signal as a function of the degree of dissociation of the hydrogen in the active volume of the ion gauge.

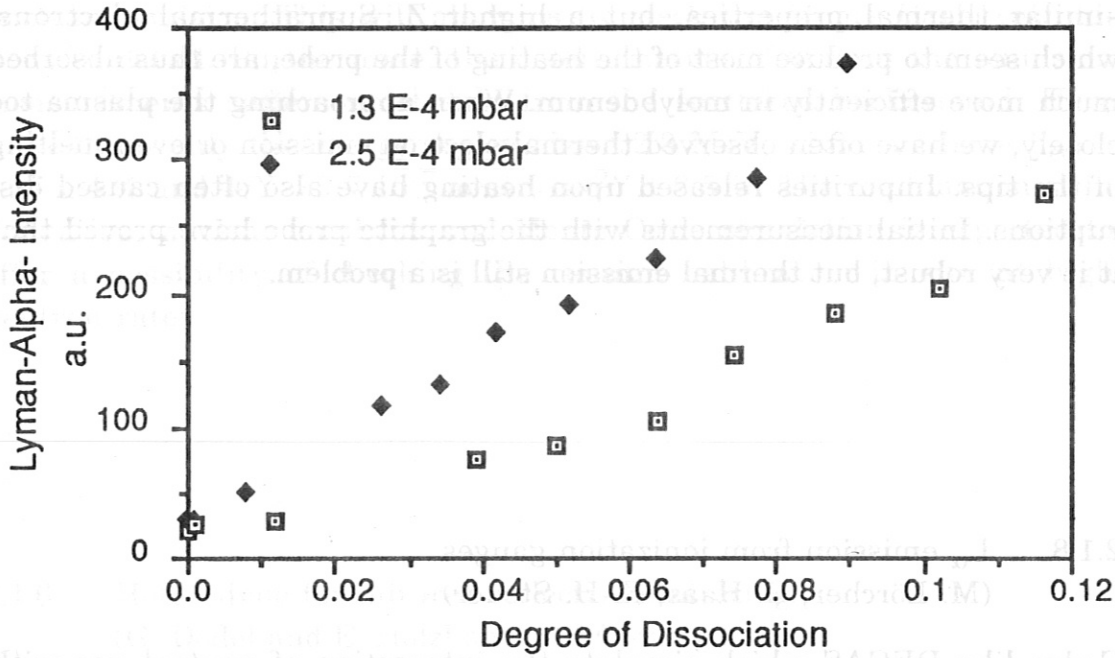

Fig. 6: L_α intensity as a function of the degree of dissociation of the hydrogen in the ion gauge for two different pressures.

2.1.9 Reflectometry
(G. Siller and F.X. Söldner
in collaboration with University of Lisbon and
the Central Technical Services of IPP)

Microwave reflection at cutoff layers inside a plasma is a rather new diagnostic method to measure density profiles in the gradient region. For this purpose three frequency regions were chosen for ASDEX with the following variations:

Region 1: From 18.0 GHz to 26.5 GHz (K-band), i.e. cutoff densities from $4.0 \cdot 10^{12}$ to $8.7 \cdot 10^{12}$ cm^{-3} (YIG oscillator).

Region 2: From 26.5 GHz to 40.0 GHz (K_α-band), i.e. cutoff densities from $8.7 \cdot 10^{12}$ to $1.9 \cdot 10^{13}$ cm^{-3} (YIG oscillator).

Region 3: From 40.0 GHz to 60.0 GHz (U-band), i.e. cutoff densities from $1.9 \cdot 10^{13}$ to $4.4 \cdot 10^{13}$ cm^{-3} (backward wave oscillator).

The frequency in each region is changed according to a sawtooth function of variable length in time. For each region a focusing hog-horn transmitter antenna is mounted on the low-field side of the plasma (Fig. 7). The microwave signals reflected from the cutoff layers in the plasma gradient regions are received by the same antenna system and results were obtained by measuring the phase shift between the reflected wave and a

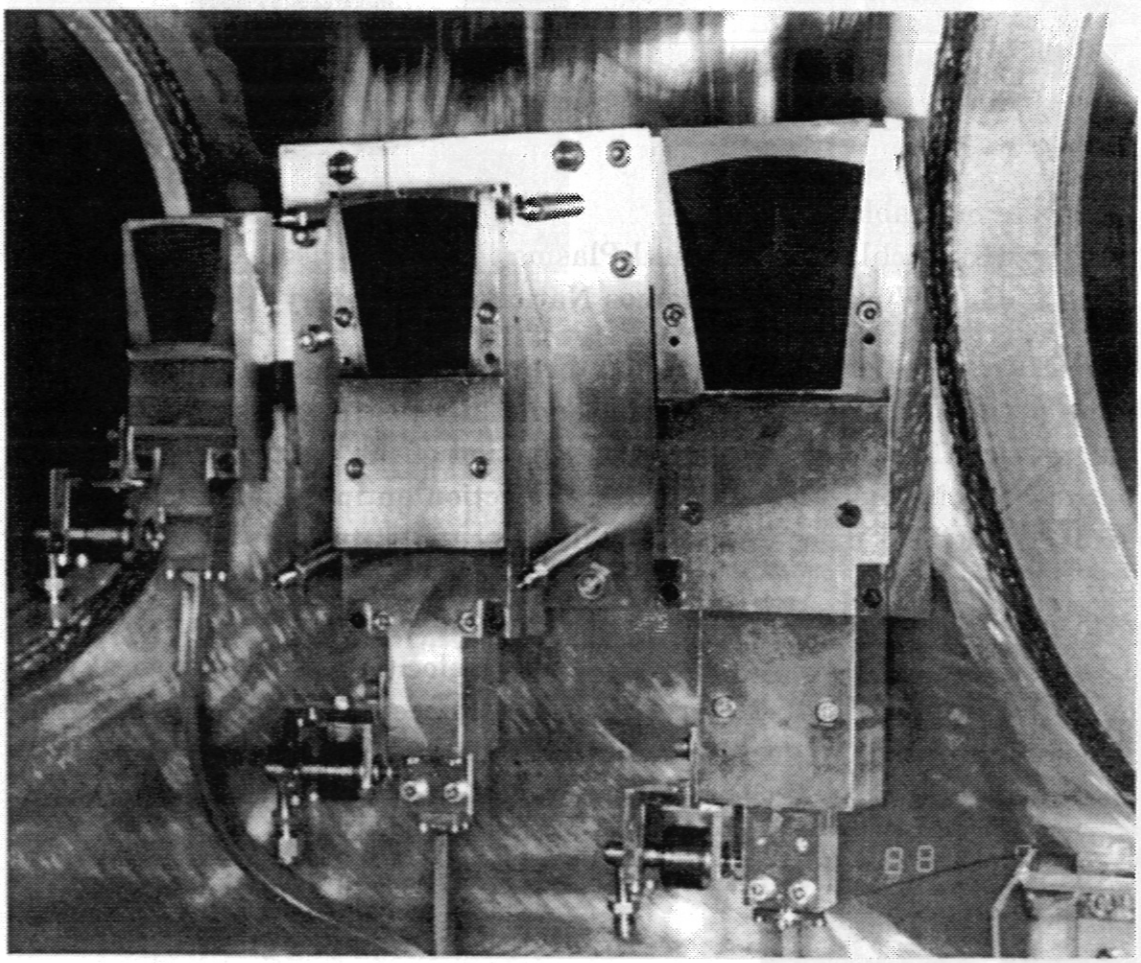

Fig. 7: Focussing hog-horn antennae for reflectrometry.

reference signal. The last one is produced by a movable pin partially inserted in the waveguide at the throat of the hog-horns (see Fig. 7). This arrangement avoids phase errors due to thermal effects of the rather long copper waveguides. The same antenna system is being prepared for mounting on the high-field side of the plasma.

In addition to the density profile measurements, also low-frequency density fluctuations in the range $f \leq 1$ MHz and their relations to the transport behaviour are to be studied. The third aim of reflectometry is to investigate high-frequency density fluctuations with the frequency of lower hybrid waves excited in ASDEX (2.45 GHz) in order to study the propagation of lower hybrid waves inside a plasma.

First density profile measurements were carried out in December 1988 with encouraging results.

2.1.10 Pellet ablation

(K. Büchl (Experimental Plasma Physics Division 1),
G.A. Wurden (Los Alamos National Laboratory, USA))

Deflection of pellets in the toroidal direction mainly during the last third of its path was observed in OH, NI and ICRH discharges by photographic diagnostics. The deflection is in the direction of the electron drift (Fig. 8a, b) except in NI discharges with beam injection antiparallel to the electron drift. In such NI discharges the pellet trace is straighter or even curved in the direction of neutral beam injection (Fig. 8c). The strongest torodial deflection observed on ASDEX (Fig. 8d) is near 90°. If we assume a constant radial pellet velocity, toroidal pellet velocities of up to several km/s near the end of the trajectory can be estimated from the photographs. These high toroidal velocities might be explained in terms of acceleration due to unbalanced ablation in the toroidal direction. However if a reduction of the radial pellet speed, as observed sometimes in time-resolved pictures is taken into account, then much slower toroidal velocities would be estimated.

Time-resolved pictures of the pellet clouds are taken with a multiply-gated CCD camera (Fig. 9a) looking down on the pellet track from an angle of

about 45 degrees. Densitometer lineouts along the toroidal axis show a dark central region in the cloud about 2 cm in diameter (Fig. 9b) in agreement with observations in time-integrated pictures. The cross-field dimensions of the light-emitting cloud are ~2 cm in diameter, while in the field direction the FWHM diameter is 5-7 cm. In the outer region of the plasma the pellet speed is constant and equal to the injection velocity, but in various discharges for the last third of the pellet paths both increased and decreased radial velocities are calculated from the CCD camera images.

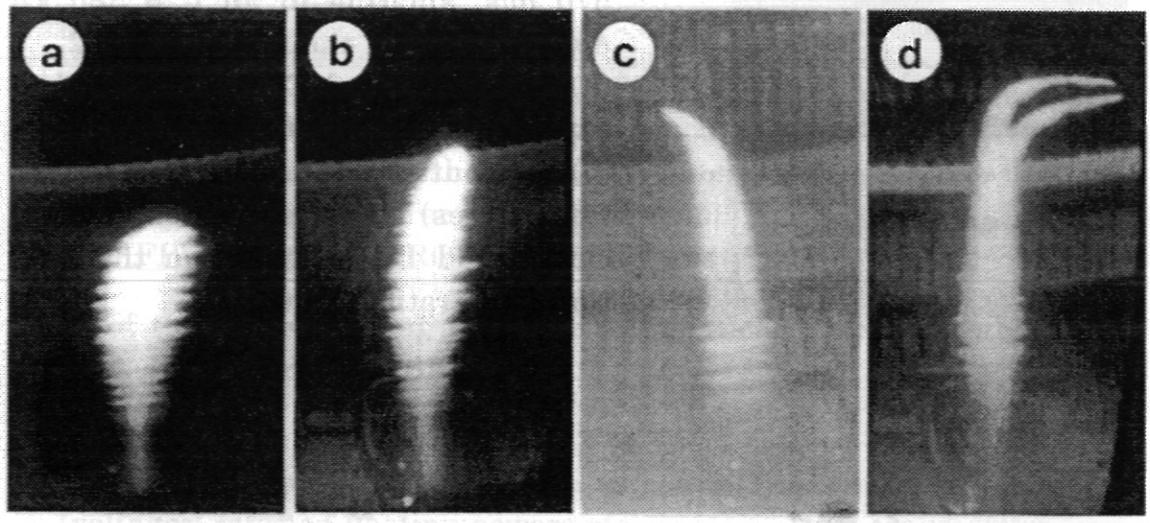

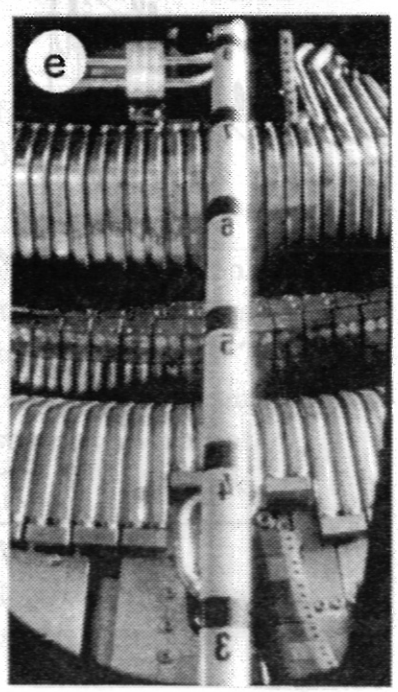

Fig. 8:

Top-view, time-integrated ASDEX pellet photos. (a) Ohmic I_p = 350 kA, B_t = 2.49 T, $\bar{n}_e = 3.4 \cdot 10^{13}$ cm^{-3}, "small" pellets, (a) first pellet and (b) fourth pellet. (c) 2.6 MW neutral injection, curvature in the ion drift direction. (d) Strongest pellet curvature seen in ASDEX. (e) Reference photo, with radial calibration rod, marks every 10 cm. The diameter of the rod is 28.5 mm. The r = 40 cm position is at the inner edge of the black mark, just above the inverted "3" on the rod (owing to lenses, the photos are inverted left-right).

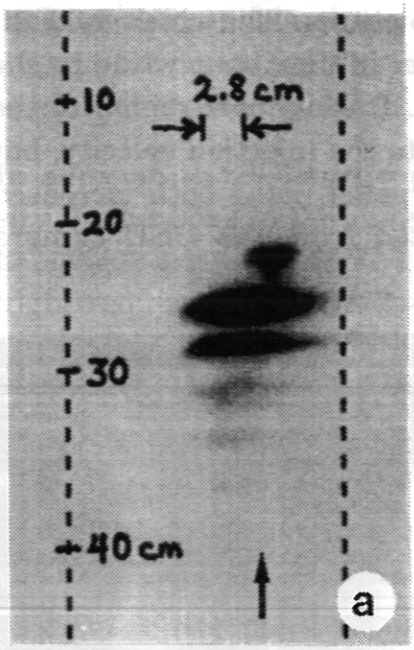

Fig. 9:

Deuterium pellet ($4 \cdot 10^{19}$ D^0 atoms) at 570 m/s, ablating in an I_p = 380 kA diverted ASDEX ohmic shot # 26082.
(a) Multiply-gated CCD picture (2 μs exposure every 50 μs).
(b) Lineouts of the elongated (along field lines) cigar-shaped emission clouds and D_α emission on the dual time/penetration depth axis.

b

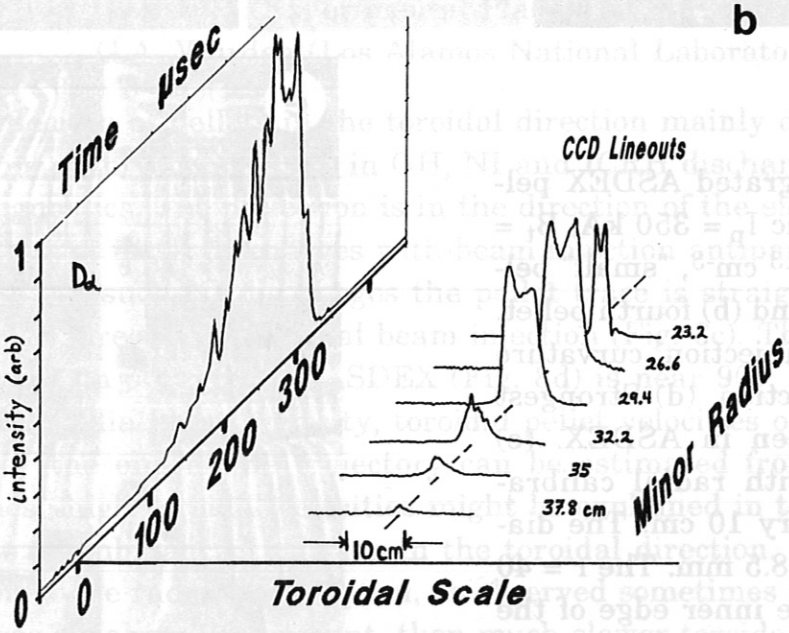

2.2 ASDEX integrated data archive system (AIDA)-DABA/SAS

(K. Grassie, O. Kardaun, K. Lackner, P. Martin, D. Pohl, U. Rang (Theory Division 3), V. Mertens (Experimental Plasma Physics Division 1))

An archive system for ASDEX shot data (DABA) was developed and installed on the IBM computer of IPP Computer Centre. Data can be addressed interactively and/or online. In the latter case the user is guided through the several DABA functions by a comfortable menu. The data archive consists of five subfiles containing 'semi-raw' as well as processed data.

Subfile 0:

- time independent global parameters, such as pellet, heating and diagnostic information. Furthermore, this subfile contains important parameters at three characteristic time points and correction factors of the FPYAG, MULTIPRO or HCEPRO analysis.

Most of the corresponding data are automatically updated when other subfiles are loaded in DABA.

Subfile 1a:

- time-dependent scalar data, such as geometrical characteristics, loop voltages, injected heating powers etc.

Subfile 1b:

- time-dependent scalar data, based on the profile data (subfile 2), e.g. averaged densities, confinement times, Z_{eff}, β, q_o etc.

Subfile 2:

- time-dependent profile data for electron temperature and density, as well as bolometrically measured power densities. The profiles are interpolated and given at 9 radial positions within the plasma. The scrape-off layer behaviour is described by fall-off lengths (temperature, density) or by a 10th radial point outside the separatrix (radiated power density).

Subfile 3:

- time-dependent profiles of temperature and electron density obtained from Thomson scattering (uninterpolated data, 16 points per profile).

Internally, DABA automatically calculates and stores the consequences of a modifiation in all relevant subfiles and creates a new shot-file version.

This guarantees that data are always consistent and allows comparison of several modified versions, if necessary. Information on the creation date and the user responsible for loading the subfile are stored within each subfile.

At present 600 shots are available in DABA. With the recently acquired disc from the Computer Centre at least 2000 discharges can be permanently stored. Statistical analysis can be performed by means of the power-ful statistical package SAS. With the DABA-SAS interface one can gener-ate standard SAS files containing DABA information. These files can easily be further processed within SAS. In the future it is intended to generate automatically each night a copy of the whole database in SAS, a system which is being successfully applied in the multi-user environment at JET.

Especially the ASDEX pellet group have been successfully using the DABA-SAS system this year.